



CFD-DEM-based Numerical Simulation of Erosion Characteristic of Multistage Pressure Relief String Regulating Valve

G. Ou¹, X. Cao¹, C. Wang¹, A. Duan¹ and H. Jin^{1,2†}

¹ The Flow Induced Corrosion Institution, Zhejiang Sci-Tech University, Hangzhou 310018, China

² Key Laboratory of Fluid Transmission Technology of Zhejiang Province, Zhejiang Sci-Tech University, Hangzhou 310018, China

†Corresponding Author Email: haozhe2007@163.com

(Received December 20, 2021; accepted March 17, 2022)

ABSTRACT

The regulating valve applied in coal liquefaction systems becomes seriously worn and its service life decreases because of a significant difference in pressure and solid–liquid flow. This study proposes a wear-resistant multistage pressure relief string-regulating valve, and examines the characteristics of depressurization of flow and the erosion of its throttle element by using computational fluid dynamics (CFD) simulations and the discrete element method (DEM) combined with the E/CRC (Erosion/Corrosion Center) erosion model of the WC-Co coating. The influence of different sizes of the opening of the valve and varying differences in pressure on the characteristics of erosion is analyzed. Moreover, properties of collisions between particles (such as the particle impact velocity and mass per second) are used to represent and analyze the characteristics of erosion. The numerical results show that the cylinder, flat, and bevel of the valve are at high risk of erosion. The characteristics of erosion of the multistage pressure relief string-regulating valve studied in this paper can provide a reference for optimizing methods of erosion prevention.

Keywords: Multistage depressurization; Regulating valve; String valve; CFD-DEM; Erosion characteristic; Solid–liquid flow.

NOMENCLATURE

AFC	Annular Flow Channel	F_S	particle shape factor
$A_{surface}$	surface area of cell geometry	F_n	normal contact force (N) tangential
BO1-BO3	bevel orifice	F_t	contact force
BH	Brinell Hardness	g	gravitational acceleration
C	erosion model empirical constant	m_p	mass of single particle
C1-C3	outer cylindrical wall of annular flow channel	N_p	number of particles hitting the cell face
C_d	coefficient of particle drag force	O1-O3	throttling flow channel
d_p	particle diameter	OO1-OO3	orthogonal orifice
ER	relative erosion rate	R, R1, R2	particle radius
$Erosion$	general erosion rate	Re	particle Reynolds number
F^{\rightarrow}	additional acceleration	\vec{u}_p, V_p	particle velocity
\vec{F}_{drag}	drag force on the particle	\vec{u}	fluid velocity
		∇P	pressure gradient
<i>Greek letter</i>			
θ Particle	impact angle	ζ_n	normal overlap of particle
μ Dynamic	viscosity of liquid phase	ζ_s	tangential overlap of particle
		ρ	density of liquid phase

1. INTRODUCTION

The control valve for the liquefaction of coal is located at the bottom of a high-temperature and high-pressure separator, and the medium of the valve contains hard solid particles. There is a large difference in pressure between the front and rear of the valve, and flow changes rapidly at its throttle, which is thus often seriously eroded (Charles *et al.* 1981; Krishnan 1984). Therefore, it is important to accurately predict the distribution of erosion over the throttling element of the control valve.

The multistage depressurization structure of the valve can enable its smooth depressurization to reduce the high-speed flow caused by the excessive pressure gradient, thus protecting the throttling element and the entire pipeline. A multistage pressure-reducing valve has been designed that can ensure high-speed flow and stable pressure relief (Du *et al.* 2014). The characteristics of the drop in pressure of a labyrinth disk valve have also been investigated and the results show that it can avoid cavitation (Wang *et al.* 2016). CFD simulations were used to examine the depressurization characteristics of a multistage orifice based on knowledge of structural optimization and noise in a high-temperature and high-pressure steam pressure-reducing valve, and a better design of the parameters of the orifice was proposed (Qian *et al.* 2016).

Computational fluid dynamics (CFD) simulation is an efficient and economical mean of studying fluid dynamics. Many researchers have used CFD to study the flow field and characteristics of erosion of complex throttling models to predict areas that are at high risk of failure. The accuracy of erosion prediction is affected by the accuracy of the erosion model and simulation of the flow field (Paggiaro *et al.* 2013). The Euler–Euler method and the Euler–Lagrange method provide different predictions pertaining to erosion (Messa *et al.* 2015), and the EL method can save more computational resources without sacrificing accuracy. Optimizations of the throttle section based on CFD and the response surface method can reduce the rate of erosion by 30.2% (Wang *et al.* 2015). The erosion distribution of a jet servo valve was investigated by using the RANS combined with Oka’s erosion model, and the life equation related to particle proportion was proposed (Yan *et al.* 2020). The particle size and difference in pressure have a significant effect on particle motion (Liu *et al.* 2019). Regions with a high intensity of turbulence can cause random particle collisions that increase erosion (Darihaki *et al.* 2017). The erosion morphology of the control valve in a steam turbine with gas–solid medium and the critical size of the maximum amount of erosion were obtained by the Euler–Lagrange method (Cao *et al.* 2020). This method when used with a large-scale dynamic mesh delivers good performance in simulating the characteristics of erosion of the control valve (Zheng *et al.* 2019). Cavitation and erosion are also significant in the butterfly valve (Liu *et al.* 2017). The erosion characteristics of the nozzle flapper of a servo valve have been examined by numerical

simulations to calculate the service life of the valve based on the predicted erosion in it (Chu *et al.* 2020). The DPM model has been used to track particles by parcels to reduce the cost of calculation, but this also reduces accuracy.

As an explicit method for the numerical analysis of discrete elements, the discrete element method (DEM) can track single discrete elements, such as rocks and small particles, and examine their dynamic characteristics. It is often used to study particle motion and collision, and to calculate the momentum, mass, and heat of particles. The CFD-DEM has delivered good performance in simulations of solid transport in fractures of complex geometry (Akhshik and Rajabi 2021; Chen *et al.* 2014). Lin *et al.* (2020) simulated the characteristics of erosion and particle distribution of the wall of a gate valve in case of openings and particles of different sizes. Akhshik *et al.* (2016) used the CFD-DEM and the Hertz–Mindlin contact model to examine the influence of three kinds of non-spherical particles—non-smooth spherical, disk-shaped, and cube-shaped particles—on a drill pipe, and the results showed that the concentration of ideal spherical particles was slightly higher than that of complex-shaped particles when the inclination angle of the drill pipe was small. Zhou *et al.* (2017) studied the influence of the shape of particles and the intensity of turbulence in the flow of a gas–solid mixture on the erosion of the elbow of a pipe. Erosion distributions in bends at angles of 90°, 60°, and 45° were also studied by a Fluent–EDEM coupled simulation (Chen *et al.* 2015). Verga *et al.* (2013) used the CFD-DEM and experiments to predict the erosion of a pipe in case of gas–solid flow.

Based on the failure analysis of a control valve in service in the coal liquefaction process, Jin *et al.* (2015) compared the results of the CFD-DPM simulation with the empirically obtained failure morphology, and found that the original structural control valve of the plunger had a high rate of local erosion as well as cavitation-induced erosion because of a single-stage drop in pressure. This study proposes a wear-resistant multistage pressure relief string-regulating valve with a long service life. The CFD-DEM is applied to study the erosion of cylindrical particles over the elbow of the valve in case of solid–liquid flow. The effects of different particle sizes and radii of curvature of the elbow on erosion and particle collisions are discussed. The particle collisions, motion, and erosion are accurately predicted (Liu *et al.* 2022). The numerical simulation results of the liquid phase flow field and discrete element in the throttling element are calculated by CFD-DEM method, which can provide reference and guiding opinions for preventing erosion and optimization of the structure.

2. MODEL SPECIFICATIONS

2.1 Problem Description

The process of coal liquefaction is shown in Fig. 1. The control valve for coal liquefaction is located at

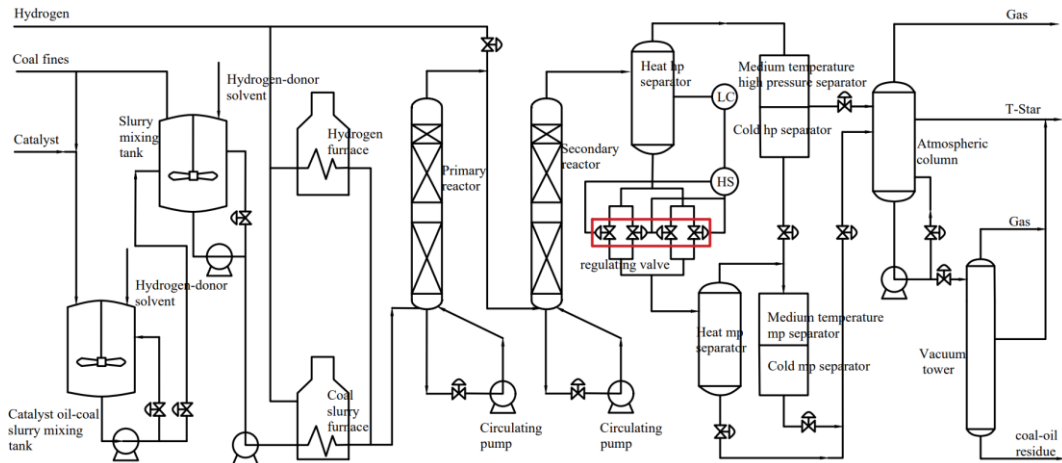


Fig. 1. Process of coal liquefaction.

the bottom of a high-temperature and high-pressure separator that regulates the discharge flow and the height of the liquid (its position is shown in the red box in Fig. 1). The control valve of the plunger in the system for coal liquefaction undergoes serious local erosion that can lead to failure due to the mixture of coal oil slurry and solid pulverized coal as well as the large differences in temperature and pressure in it (Jin *et al.* 2015).

2.2 Model Structure

The structural model of the multistage pressure relief string-regulating valve is shown in Fig. 2. Figure 2(a) shows the overall model, which is mainly composed of a seat, cover, stem, core and sleeve for the core of the valve. Figure 2(b) shows the direction of flow of the internal flow channel from two sections. The flow channel is mainly composed of four annular flow channels and three pairs of throttling channels. Each throttling channel is composed of two throttling structures: namely, the bevel orifice (BO) and the orthogonal orifice (OO). As shown in Fig. 2(b), each throttling channel and annular flow channel is referred to as O1–O3 (the bevel orifices and the orthogonal orifices are denoted respectively by BO1–3 and OO1–3) and AFC 1–AFC 4, respectively, from the positive to the negative direction of the X-axis. The direction of flow is indicated by the red arrows in Fig. 2(b) (the blue part represents the flow channel).

The value of H shown in Fig. 2(c) is the distance between the plane of the core of the third throttling section and the plane of the sleeve of the core. When the valve is opened up to 80%, 65%, 50%, 35%, and 20%, the values of H are 3.96 mm, 6.93 mm, 9.9 mm, 12.87 mm, and 15.84 mm, respectively.

The model was meshed by using the poly-hexcore method. The grid independence test is shown in Figs. 3(a) and (b), where the former shows the maximum velocity distribution of the continuous phase along the X-axis under different numbers of grids in Fluent. The grids used in the EDEM are independent of Fluent, whereas the grid size significantly influences the calculated erosion. Figure 3(b) shows the

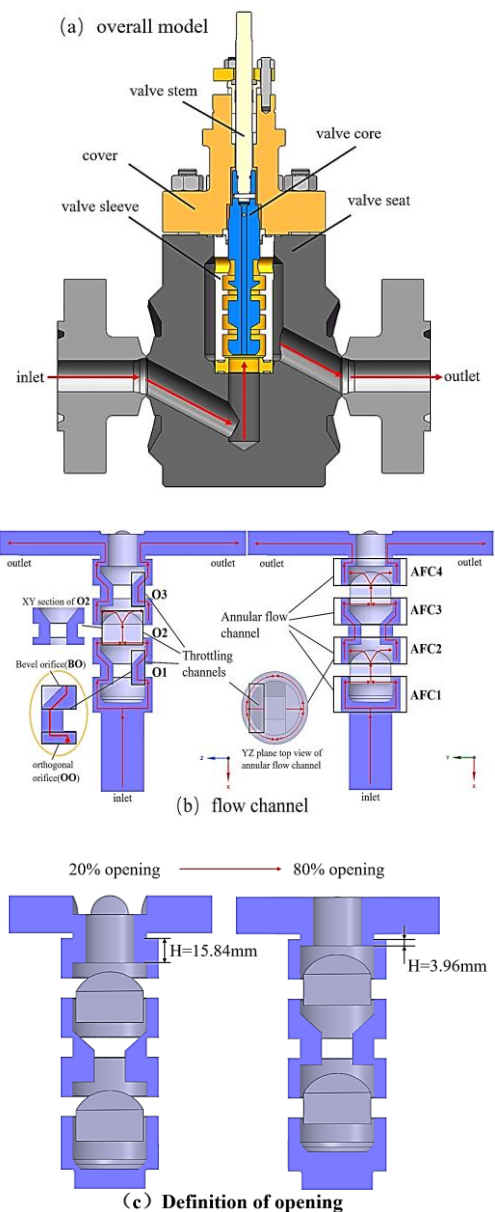
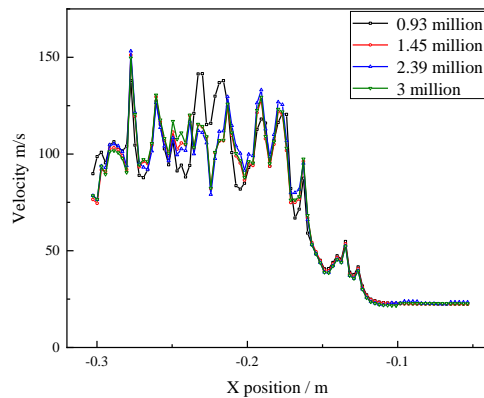
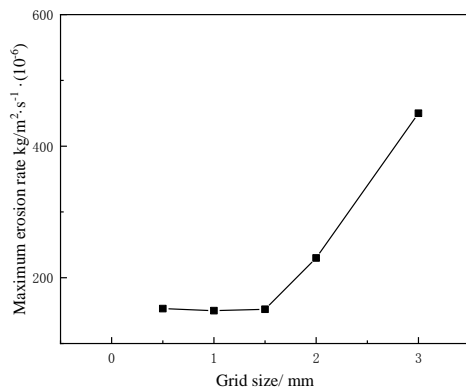


Fig. 2. Structure of multistage pressure relief string-regulating valve.

maximum rate of erosion of the cylindrical surface of the annular channel under different grid sizes of the EDEM. The results included the velocity distribution of the continuous phase calculated by using varying numbers of cells. As they were relatively close, we used 1.45 million cells for calculation. The erosion model was compiled in the EDEM by using its contact model API. It was called every time the particles came into contact with the grid surface. When the grid was larger, more particles came into contact with its surface, and the rate of erosion accumulated within one grid to lead to a high rate of local erosion. For the EDEM grid, we set 1.5 mm as the minimum grid size to ensure the accuracy of the calculated erosion.



(a) Verification of the mesh used in Fluent



(b) EDEM grid verification

Fig. 3. Grid independence test.

2.3 Numerical Model

2.3.1 Modeling the continuous phase

The incompressible RANS method is used to solve for the continuous flow. RANS is a method to transform the problem of unsteady and multiscale turbulence into one of time-averaging flow. The equations of continuity and momentum can be written as:

Continuity:

$$\frac{\partial \rho}{\partial t} + \nabla \cdot (\rho \vec{v}) = 0 \quad (1)$$

Momentum :

$$\frac{\partial}{\partial t} (\rho \vec{v}) + \nabla \cdot (\rho \vec{v} \vec{v}) = -\nabla p + \nabla \cdot (\vec{\tau}) + \rho \vec{g} - F_{\text{drag}} \quad (2)$$

$\vec{\tau}$ is a stress tensor and F_{drag} is the drag force between the continuous and the discrete phases.

RNG k-ε is the turbulence model used to solve for continuous flow, and a standard wall function is used. The effect of swirl on turbulence is included in the RNG model to enhance the accuracy of modeling swirling flows to a greater extent than the standard *k-ε* model. Compared with another two-equation model, *k-ω*, the requirement for meshing the boundary layer is looser in the standard wall function.

2.3.2 Discrete Phase Modeling

The coupled calculation process of the Fluent-EDEM method is shown in Fig. 4. The EDEM is a software established based on the DEM that can track single discrete particles rather than parcels to yield more accurate results. Its calculation of the particle-particle contact force and the particle geometry is based on the mechanics of the given materials. The exchange of momentum between the fluid and the particles is solved for by the DPM in Fluent. The equation of the force balance of particles can be written as:

$$m_p \frac{d \vec{u}_p}{dt} = m_p \vec{g} + \frac{\vec{u} - \vec{u}_p}{\tau_r} + \vec{F} \quad (3)$$

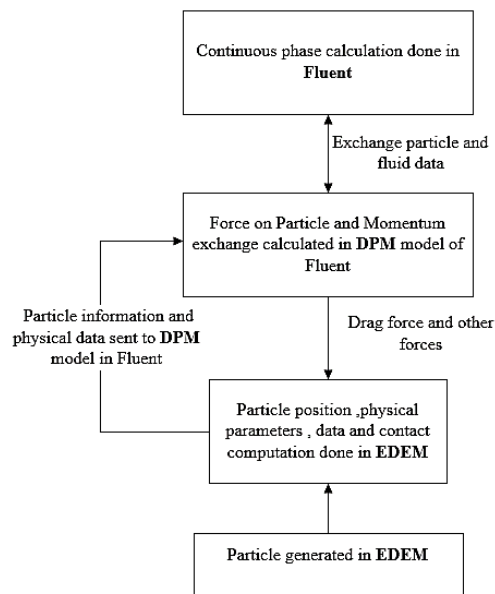


Fig. 4. Coupled Fluent-EDEM calculation.

\vec{F} is an additional acceleration (including the virtual mass force, pressure gradient force, lift force,

and impact force), $\vec{F}_{drag} = \frac{\vec{u} - \vec{u}_p}{\tau_r}$ is the drag force per unit mass of particle, and

$$\tau_r = \frac{\rho d_p^2}{18\mu C_d Re} \quad (4)$$

The drag coefficient C_d has been given by [Morsi and Alexander \(1972\)](#).

When a particle collides with another or the wall, tangential and normal forces act on each other. According to the Hertz–Mindlin (no-slip) model ([Johnson 1985](#); [Landau and Lifshitz 1970](#); [Mindlin 1949](#)), the nonlinear normal force can be written as:

$$F_n = \frac{2}{3} k_n R^{1/2} \xi_n^{3/2} \quad (5)$$

where $R=2R_1R_2/(R_1+R_2)$. R_1 and R_2 are the particle diameters, $k_n=4G/(1-\nu)$ is the effective normal stiffness defined by shear modulus G and the Poisson ratio ν , and ξ_n is the normal overlap between grains.

Tangential force:

$$F_s = k_s (R \xi_s^2)^{1/2} \xi_s \quad (6)$$

ξ_s is the tangential displacement that takes place since contact was established and $k_s=8G/(2-\nu)$ is the tangential stiffness.

The E/CRC model for the WC-Co coating at 400 °C was used as the erosion model ([Zheng *et al.* 2016](#); [Wang *et al.* 2021](#)). It was used in the EDEM software as an API contact model:

$$ER = C(BH)^{-0.59} F_s V_p^n F(\theta) \quad (7)$$

BH is Brinell hardness, F_s is a constant shape factor, V_p is particle velocity (m/s), n is the velocity component, $F(\theta)$ is the impact angle, C is an empirical constant, 1.2×10^{-10} , $C(BH)^{-0.59} F_s$ can be defined as a constant, and n is 2.3. $F(\theta)$ is linearly fitted as:

$$\begin{aligned} 0.35 \theta^1 - 0.01 \theta^2 + 2.992 \theta^3 + \\ 0.576 \theta^4 - 0.000184 \end{aligned} \quad (8)$$

$$Erosion = \sum_{z=1}^{N_p} \frac{m_p ER}{A_{face}} \quad (9)$$

Erosion is the general rate of erosion, in $\text{kg/m}^2 \cdot \text{s}^{-1}$. m_p is the mass of a single particle impinging on the wall, A_{face} is the area of the cell, and N_p is the number of particles in contact the cell face.

2.4 Case Study

2.4.1 Verifying the numerical method

Flow regulation was realized by using multiple chokes in the multistage pressure relief string-

regulating valve. The applicability of the CFD-DEM was verified through experimental data from [Mclaury \(1996\)](#). The turbulence model used was the standard $k-\varepsilon$ and the erosion model was Mansouri’s model ([Mansouri 2016](#)) for 6061 Aluminum ([Darihaki *et al.* 2017](#)). The settings of Fluent and the EDEM are listed in Table 1. The time steps for the continuous phase and the discrete element were $2e^{-5}$ s and $2e^{-8}$ s, respectively. A schematic of the model, and a comparison between the numerical results and experimental data are shown in Fig. 5.

Table 1 Settings of Fluent and EDEM

Fluent:		
Boundary	Type	Value
Inlet	Velocity inlet	2.5 m/s
Outlet	Outflow	
Wall	No slip	
Fluid material density (water)		998.2 kg/m ³
Fluid material density viscosity		0.001003 kg/(m·s)
EDEM:		
Properties	Silica sand	6061 Al
Density/ kg/m ³	2650	2700
Poisson ratio	0.13	0.34
Young’s modulus / GPa	73	69
Coefficient of restitution	0.5	0.5
Coefficient of static friction	0.6	0.4
Coefficient of rolling friction	0.05	0.05

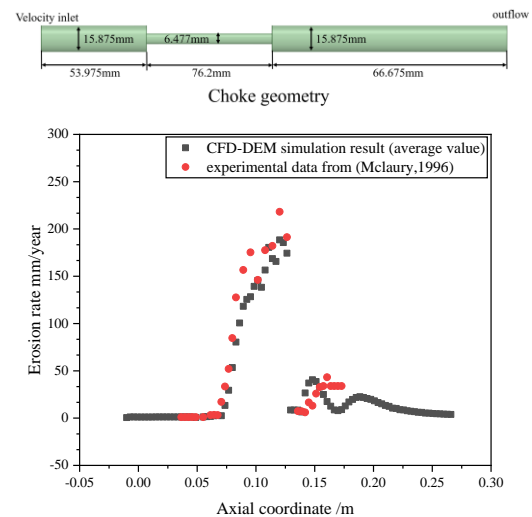


Fig. 5. Model schematic and verification of simulation.

2.4.2 Calculation settings

To investigate the characteristics of erosion of the multistage pressure relief string-regulating valve, we considered the effects of the size of its opening and the difference in pressure. The settings used for

Table 2 Settings for different cases

Case	Valve Opening	Particle Diameter/ mm	Inlet Pressure/ MPa	Outlet Pressure/ MPa	Particle Mass Flow Rate/ kg·s ⁻¹	Fluid Density / kg·m ⁻³	Fluid Viscosity / mPa·s
1	20%	0.2	18.671	2.947	0.006	731.8	0.212
2	35%						
3	50%						
4	65%						
5	80%	0.2	14.671	2.947	0.006	731.8	0.212
6	50%						
7	50%						
8	50%						
9	50%						

different cases are shown in Table 2. The properties of the materials for EDEM calculations are listed in Table 3. The coal powder contained 38.3% of silica sand particles. Silica sand was thus selected as the abrasive particle for the simulation. The properties of WC-Co were obtained from [Bernt *et al.* \(1972\)](#). The size of the timestep of the Fluent simulation was 1e-5 s and that of the EDEM simulation was 2e-7 s.

Table 3 Properties of the materials for EDEM

Properties	Silica sand	WC-Co
Density/ kg/m ³	2650	14600
Poisson ratio	0.13	0.18
Young's modulus / GPa	73	575
Coefficient of restitution	0.5	0.5
Coefficient of static friction	0.6	0.4
Coefficient of rolling friction	0.05	0.05

3. RESULTS AND DISCUSSION

3.1 Opening

3.1.1 Characteristics of continuous phase flow

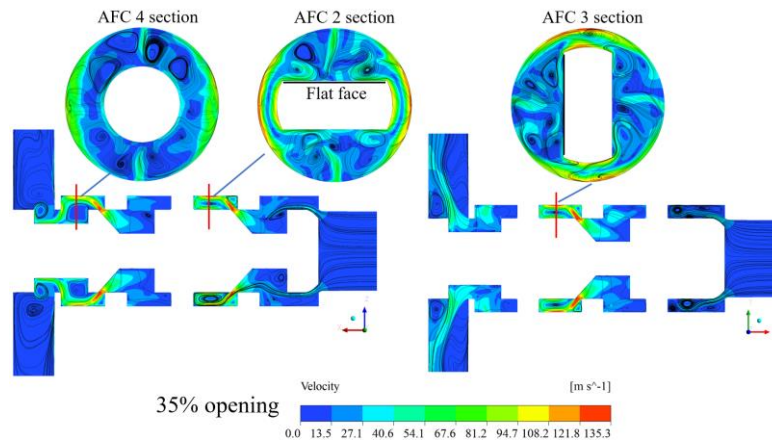
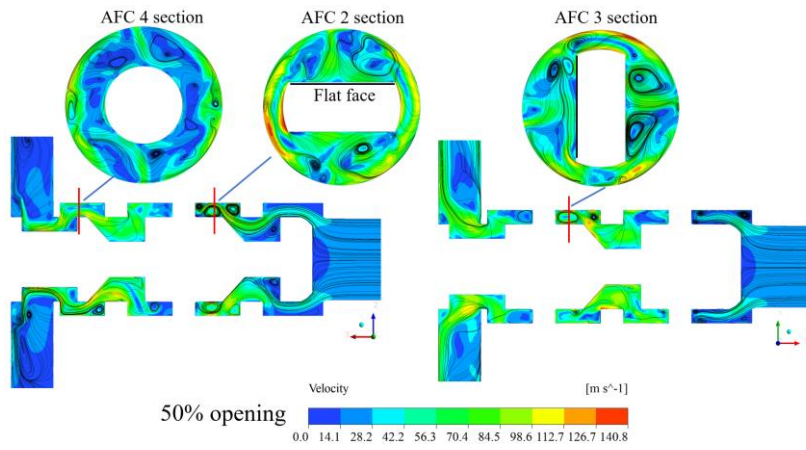
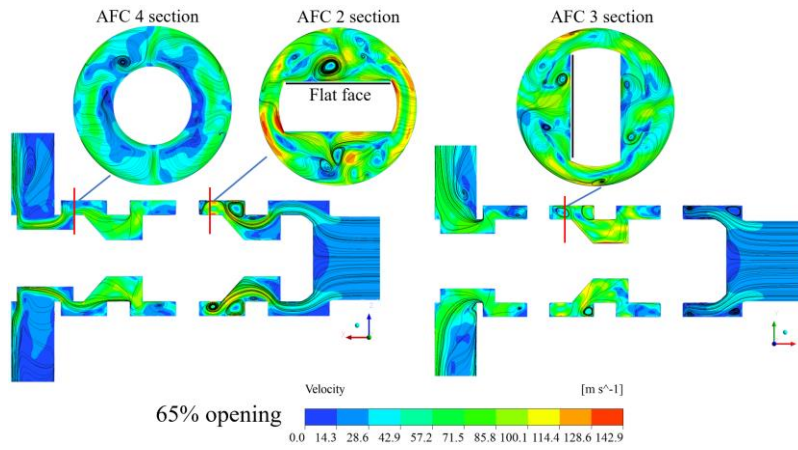
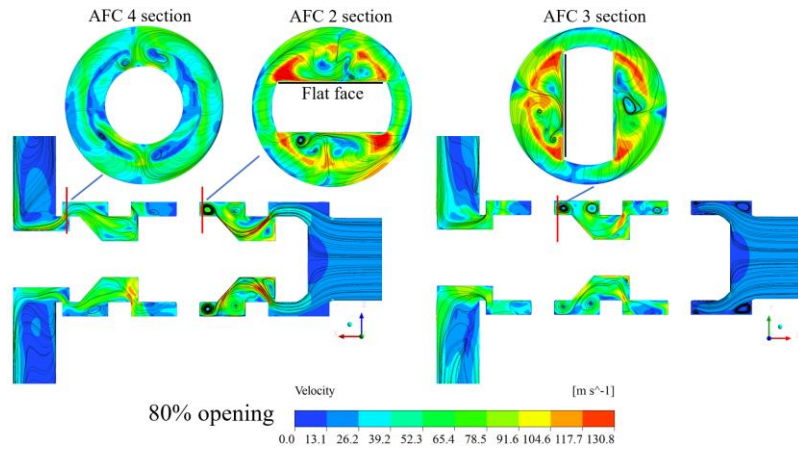
The maximum velocity contours of the two sections under openings of different sizes are shown in Fig. 6. The maximum velocity of the XY section was 142.9 m/s when the opening of the valve was at 65% of its maximum size. When liquid passed through the throttles and then impinged on the outside wall of annular flow, strong swirls were generated in the annular channels, especially at openings of the valve of 35% and 20%. As the size of the opening increased, the position of impact of the flow moved upstream. For the AFC sections, the fluid zone above the flat surface (defined in Section 3.1.2) had a stagnant velocity with openings of 35% and 20% because the part of fluid entering the AFC zone from the throttling zone tended to flow along the annular channel, and formed a shock owing to the symmetrical AFC. Moreover, the velocity of the fluid near the flat surface was lower than that in case of openings of other sizes (an opening of 80%

yielded the highest velocity). When the size of the opening was increased, the stagnation in velocity was not prominent, and this can be attributed to a reduction in the space in the zone before the BO, called the buffer zone, which reduced energy loss.

Figure 7(a) shows the maximum velocity of the fluid along the direction of flow. When the opening of the valve was larger than 50% of its maximum size, the point at which the acceleration of the fluid was high was located at the OO. When the size of the opening was 50%, it occurred both at the BO and the OO. Moreover, the flow resistance and energy loss in the throttling channel were not large enough for 50%, which is why the velocity of fluid with an opening of 50% increased along the direction of flow. When the opening was smaller than 50%, a high-velocity gradient occurred at the BO because more pressure-induced energy was converted into kinetic energy in the narrower flow channels.

Figure 7(b) shows the distribution of the turbulence intensity, from which it can be concluded that strong turbulence developed after O1, and points with a high turbulence intensity appeared in the cavity between the BO and OO, and the annular flow channels. This led to the dissipation of a large amount of kinetic energy, corresponding to the velocity in Fig. 7(a). Figure 7(c) shows the pressure distribution under openings of different sizes. The difference in pressure between the BO and the OO was large, which led to a significant drop in pressure when the fluid passed through them.

Figure 7(d) shows the mass flow distribution at the outlet of each size of the opening. Flow through the outlet decreased with the size of the opening of the valve. However, flow through the outlet with the opening was 80% was lower than those at 65% and 50% owing to the smaller area of flow of the OO, which increased the flow resistance. The mass flow rates of outlets 1 and 3 were higher than those of outlets 2 and 4. After passing through the throttling section, the high-velocity fluid was subjected to a strong shear stress when it came into contact with several corners around the boundary wall. Therefore, many vortices were formed before flow through outlets 2 and 4, leading to the dissipation of more kinetic energy. Almost no swirls were created in flows through outlets 1 and 3 after the last throttling section, and the high-velocity region was relatively stable.



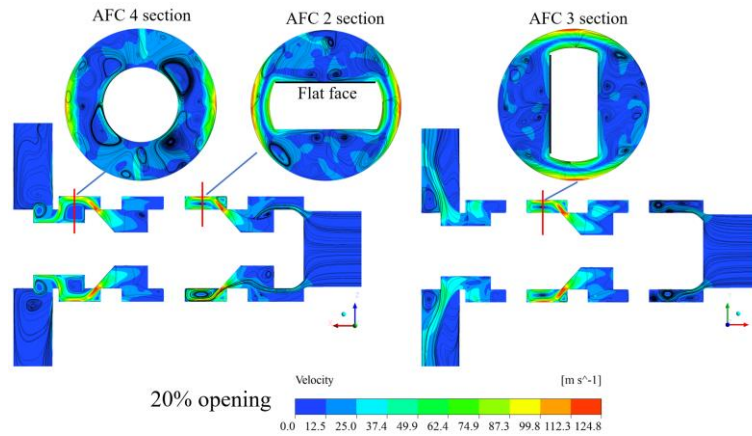


Fig. 6. Velocity contours in sections XZ, XY, and AFC of the valve with openings of different sizes.

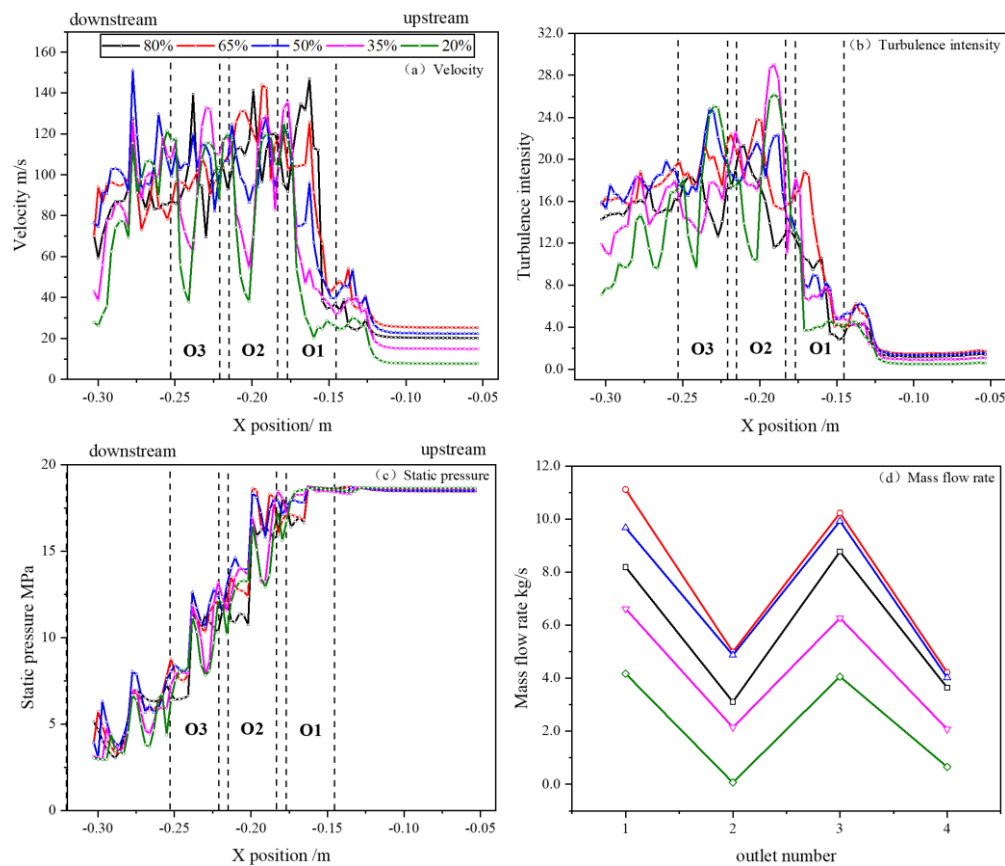


Fig. 7. Comparison of the parameters of flow with openings of different sizes.

3.1.2 Erosion distribution

To examine the area at high risk of erosion, certain parts of the throttling sections and the annular flow channels were selected for analysis. The erosion-related performance of the three parts of the valve shown in Fig. 8 was analyzed: bevels 1–3, flats 1–3 (wall of the core of the valve) and cylinders 1–3 (inner wall of the sleeve of the valve).

L_{min} and L_{max} were the minimum and maximum values, of the coordinates respectively. The length ratio is introduced to express the scale of lengths of the distributions of erosion on the cylinder,

bevel, and flat of the throttling section. it is expressed as follows:

$$Length\ ratio = \frac{L - L_{min}}{L_{max} - L_{min}} \quad (10)$$

L is the X coordinate of the cylindrical surface, and the coordinate in the Z or Y direction in the abscissa of the flat plane. The ordinate is the X direction coordinate. For the surface of the bevel, L is the Z or Y coordinate in the abscissa, and the ordinate is the longitudinal width of the surface.

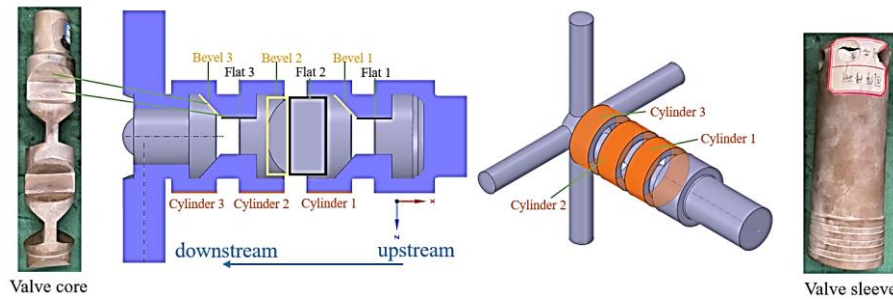


Fig. 8. Parts of the valve analyzed the erosion-related performance of which was analyzed.

3.1.2.1 Annular flow channel

Figure 9(b) shows a diagram of erosion distribution on the cylindrical surface of the annular channel for cylinders 1–3 (C1–3). The throttling channels (O1–3) for them are marked in red in Fig. 9(b). The erosion profiles of C1 and C3 were similar in shape and location but the erosion morphology of C1 was clearer. However, as the size of the opening decreased, the angular range of the area of high erosion decreased gradually from 180° to 60°. The area subjected to serious erosion gradually moved upstream along the X-axis.

The results show that the maximum erosion occurred at C1 owing to the higher velocity gradient and difference in velocity between particles at O1 compared with those at O2 and O3, where this generated a larger drag force and higher fluid flow. The maximum depths of erosion at C1 and C3 occurred at 80° and 280°, respectively. The angular position of the area of serious erosion in C2 was different from those of the other two cylindrical faces by 90°. However, when the size of the opening was 80%, the erosion morphology was different. In C2 and C3, erosion occurred at the location deviating from the throttling channel by 90°, where the particles were concentrated. Moreover, with an opening of 80%, the point of acceleration of the particles occurred at the OO, but the buffer zone between the OO and the BO led to the dissipation of a large amount of kinetic energy. This means that when the particles impacted the surface of the cylinder for the first time, their velocity decreased significantly.

A plot of erosion of the cylindrical surface under openings of different sizes is shown in Fig. 10. Figure 10(a) shows that the most severe area of erosion was located at the exits of the orifice (throttling channel). Because of the impact angle function term in WC-Co erosion model is in linear form which has higher value with bigger impact angle. When impact velocity and impact angle are both large, it will induce more serious erosion. But when the opening was 65% or 50%, the erosion was more dispersed and occurred at several points owing to high particle concentration at 90° with respect to the throttling channel.

Figures 10(d)–(f) show that vortical flow in the annular channels induced the residence of and repeated collision among particles. More particles stayed in the annular channel and fewer particles entered the next stage of a drop in pressure.

Therefore, the trends of distributions of the average rate of erosion and particle mass were clearer for C3 than for C1 and C2. This is because after three stages of a drop in pressure and the dissipation of mechanical energy, the intensity of turbulence was much lower at the exit of O3 and the stream of particles was stabler. This caused the concentration of erosion on points with a high impact velocity.

3.1.2.2 Throttling the flow channel

The erosion diagram of the flat part is shown in Fig. 11. Figure 12 shows the erosion plots of the three flats. The maximum depth of erosion occurred with an opening of the valve of 80%, and was concentrated. The erosion profile over flat 1 with an opening of 80% was different from those of other openings, and featured the maximum wear. Figure 7(a) in Section 3.1.1 shows that there was a maximum velocity at OO1 upstream of the flat, which caused the particles to suddenly speed-up and gather. This led to the concentration of particles near the wall at flat 1, resulting in concentrated wear. In Fig. 12, flat 2 with an opening of 80% had the maximum concentrations of particle mass and impact velocity, giving rise to aggressive erosion.

The erosion morphologies with openings of sizes of 65%, 50%, and 35% were similar. The former size of opening yielded the most severe erosion, and flat 2 underwent the most serious erosion followed by flat 3. Compared with openings of other sizes, the local severe erosion area of the 35% opening moved upward in the longitudinal direction and was narrowed. As the size of the opening decreased, the area of flow of the OO increased and caused the velocity of the particles to decrease significantly. This reduced erosion and the mass flow rate of the particles. Most particles impacted the flat surface from both sides, resulting in an extension of the erosion morphology along the transverse direction owing to the large area of flow through the orifice of the OO.

When the size of the opening of the valve was 20% of its maximum, fewer erosion points occurred on the flat surface. But for flats 2 and 3, local erosion was observed in the locations marked in red. Figure 12(c) shows that the velocity of particle impact was low, thus, the trend of following fluid for particles is obvious. What's more, the near-wall fluid can bring a protection for the wall, which slow down the small and low-velocity particles. Therefore, few particles hit on the wall and cause serious erosion.

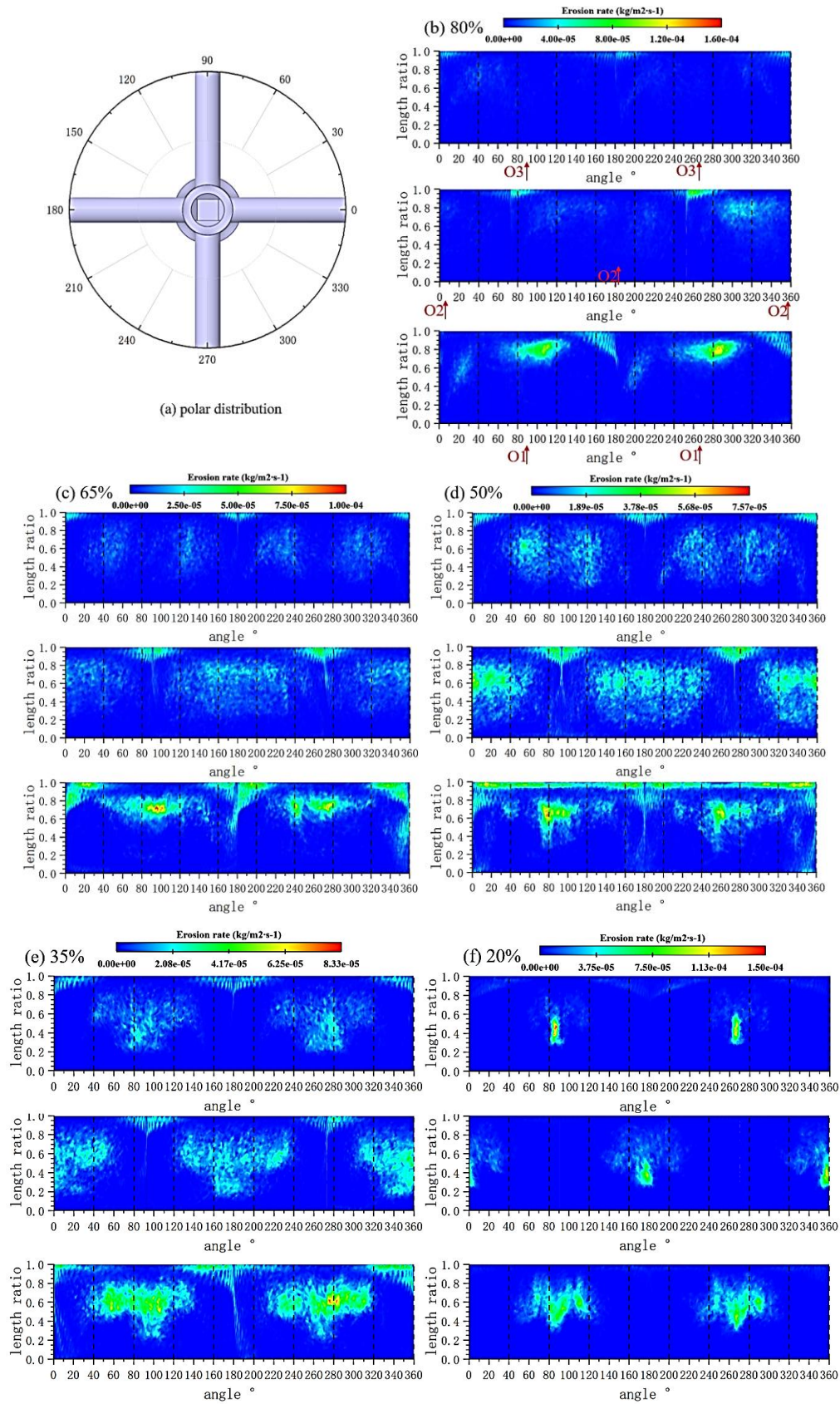


Fig. 9. Erosion profiles over the three cylinders with openings of different sizes.

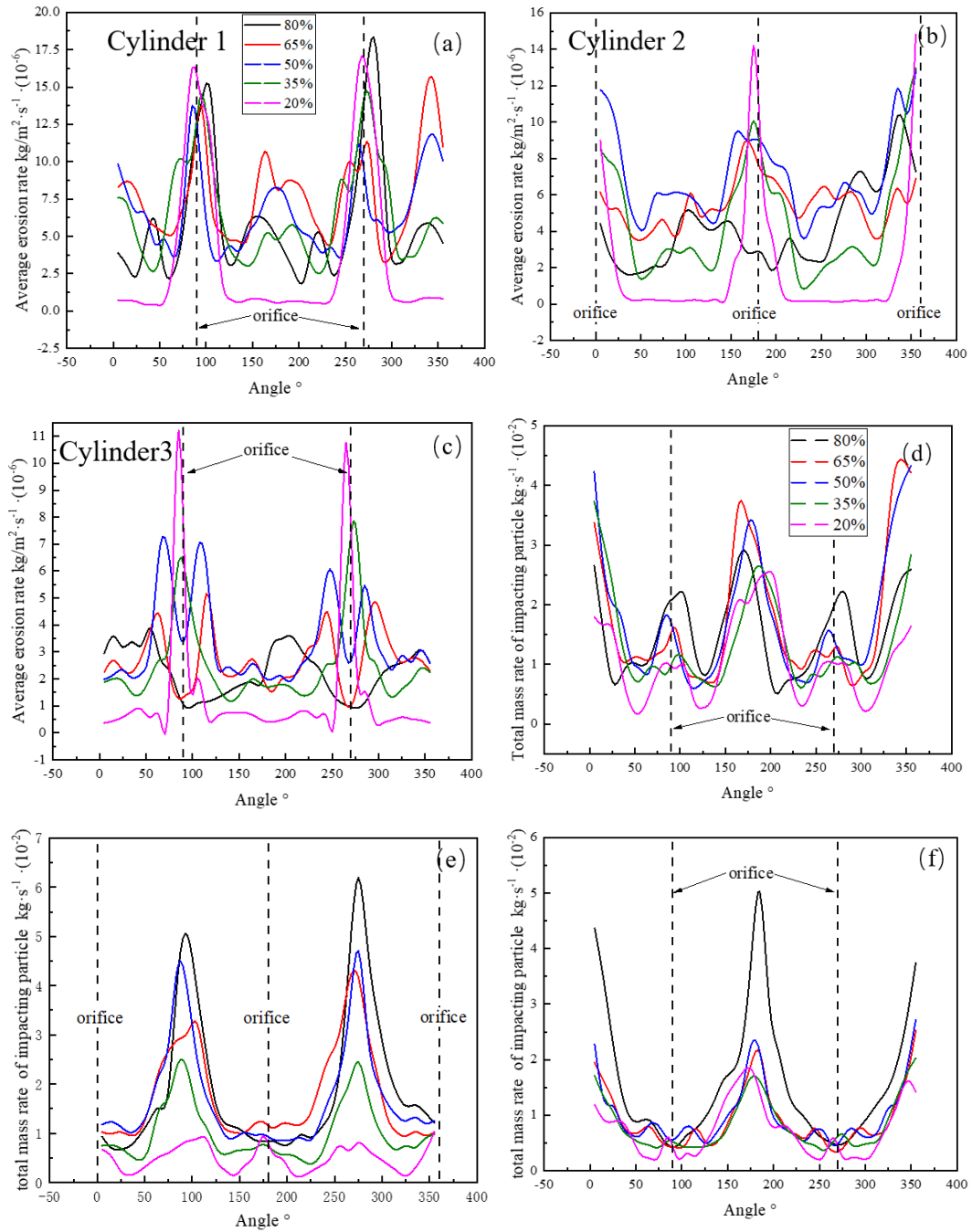


Fig. 10. Rates of erosion and masses of the particles impacting cylinders with openings of different sizes.

The erosion diagram of the bevel is shown in Fig. 13. Figure 14 shows the characteristics of erosion of the three bevels under openings of different sizes. When the opening was larger than 50% in bevel 1, the OO orifice played an important role. High-speed fluid at the OO impacted the flat at a large angle and then flowed along the boundary, driving the particles to impact the bottom of the bevel. A significant amount of erosion was thus concentrated at the bottom. With a reduction in the size of the opening and the area of flow in the BO, throttling was mainly realized by the BO section.

Figure 14(a) shows that the particle stream with a high mass concentration at the top of the bevel impinged on it at a high speed. The erosion distribution thus gradually moved up along the longitudinal direction. When the sizes of the opening were 50% and 35%, for bevel 1, the turbulence intensity of flow in O1 was small, as was energy dissipation, and thus the effect of the vortex on the particles was slight. In case of bevel 2 or 3, the turbulent effect induced a large reduction in particle velocity, because of which the location of erosion changed and its value decreased.

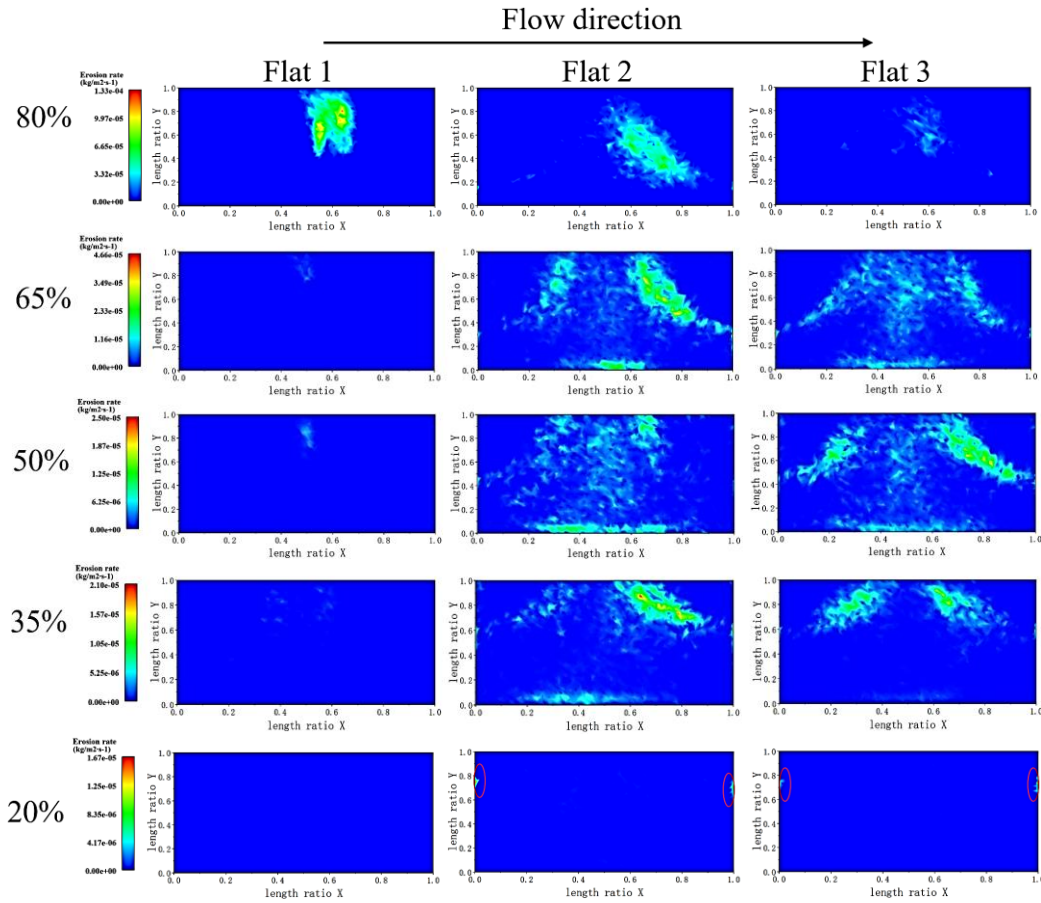


Fig. 11. Comparison of erosion profiles of flats with openings of the valve of different sizes.

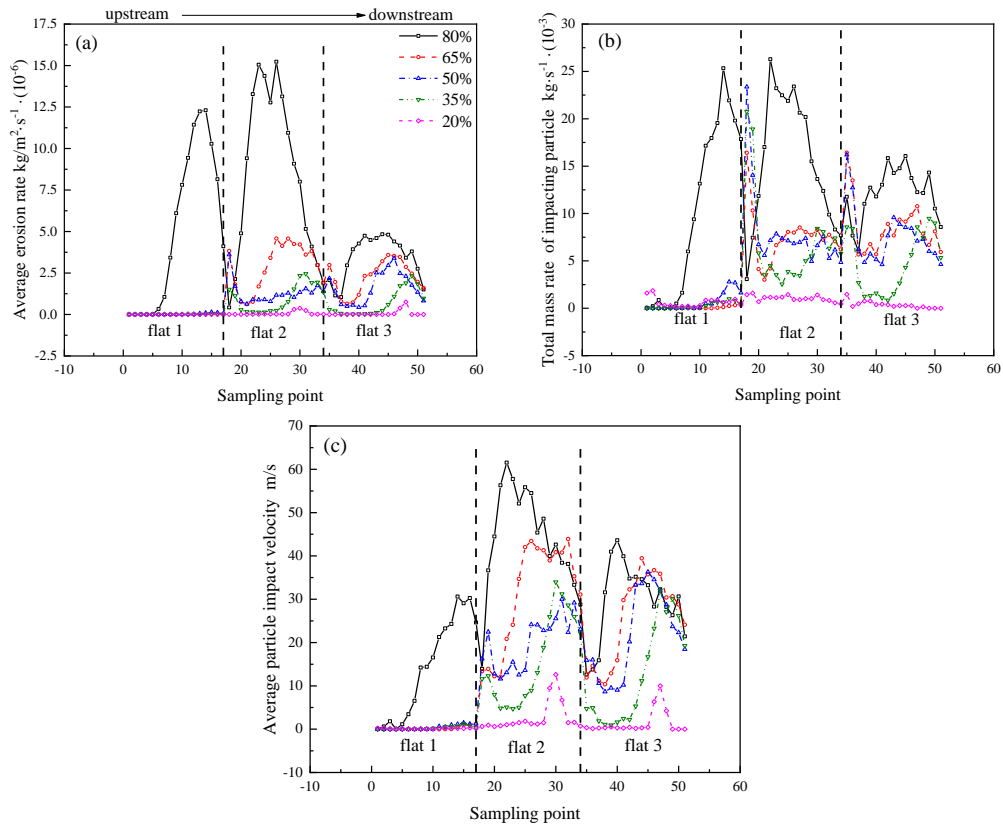


Fig. 12 Erosion characteristics of three flats with openings of the valve of different sizes: (a) average erosion rate; (b) total mass of impacting particles; (c) average particle impact velocity).

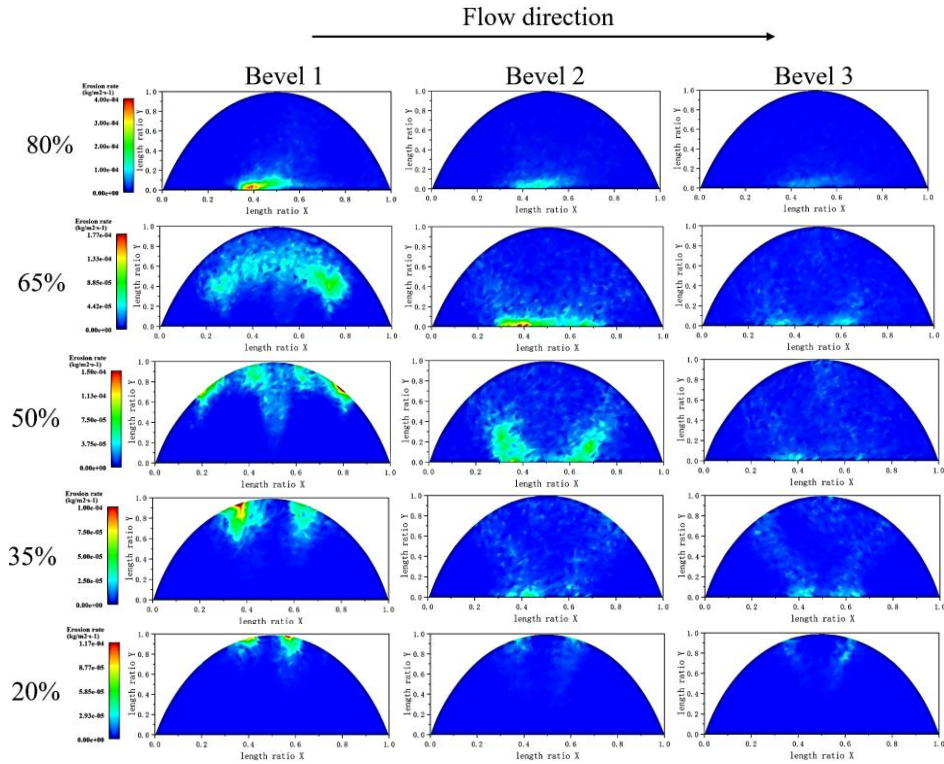


Fig. 13. Comparison of erosion profiles of bevels with openings of different sizes.

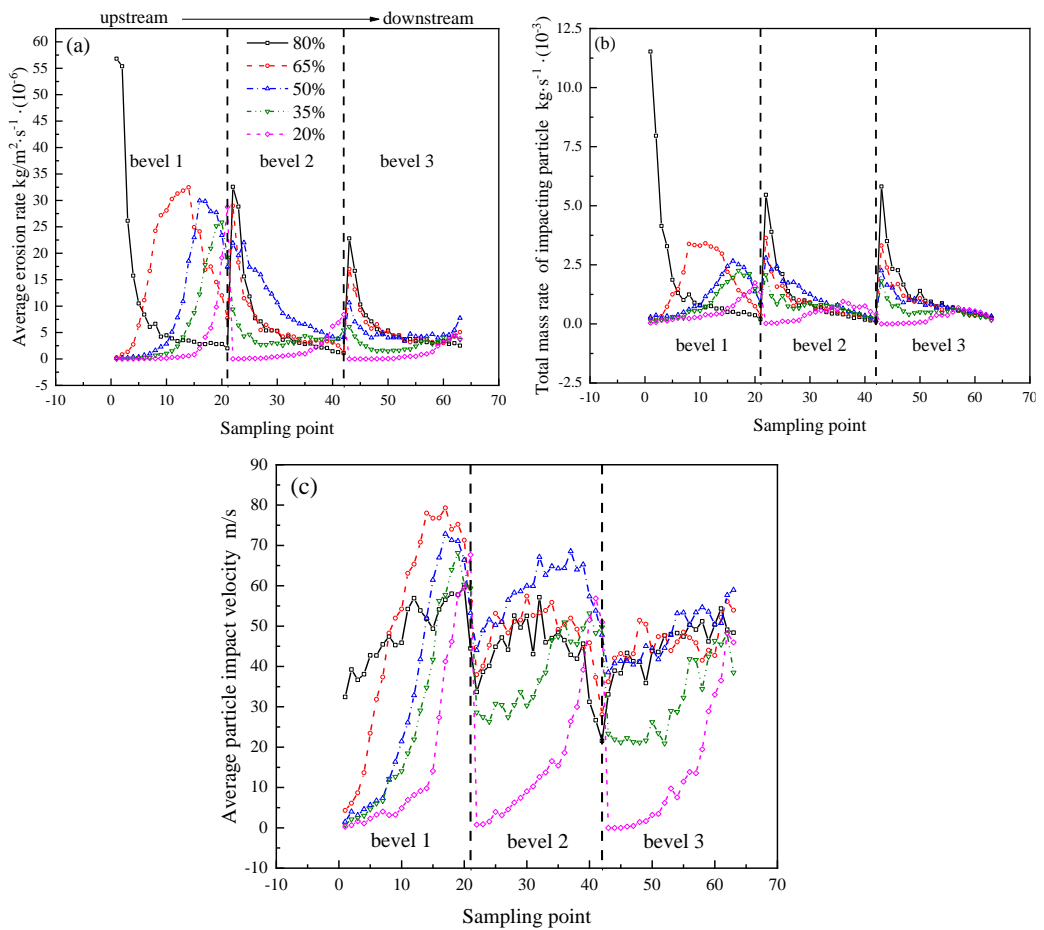


Fig. 14. Erosion characteristics of three bevels with openings of the valve of different sizes ((a) average erosion rate; (b) total mass of impacting particles; (c) average particle impact velocity)

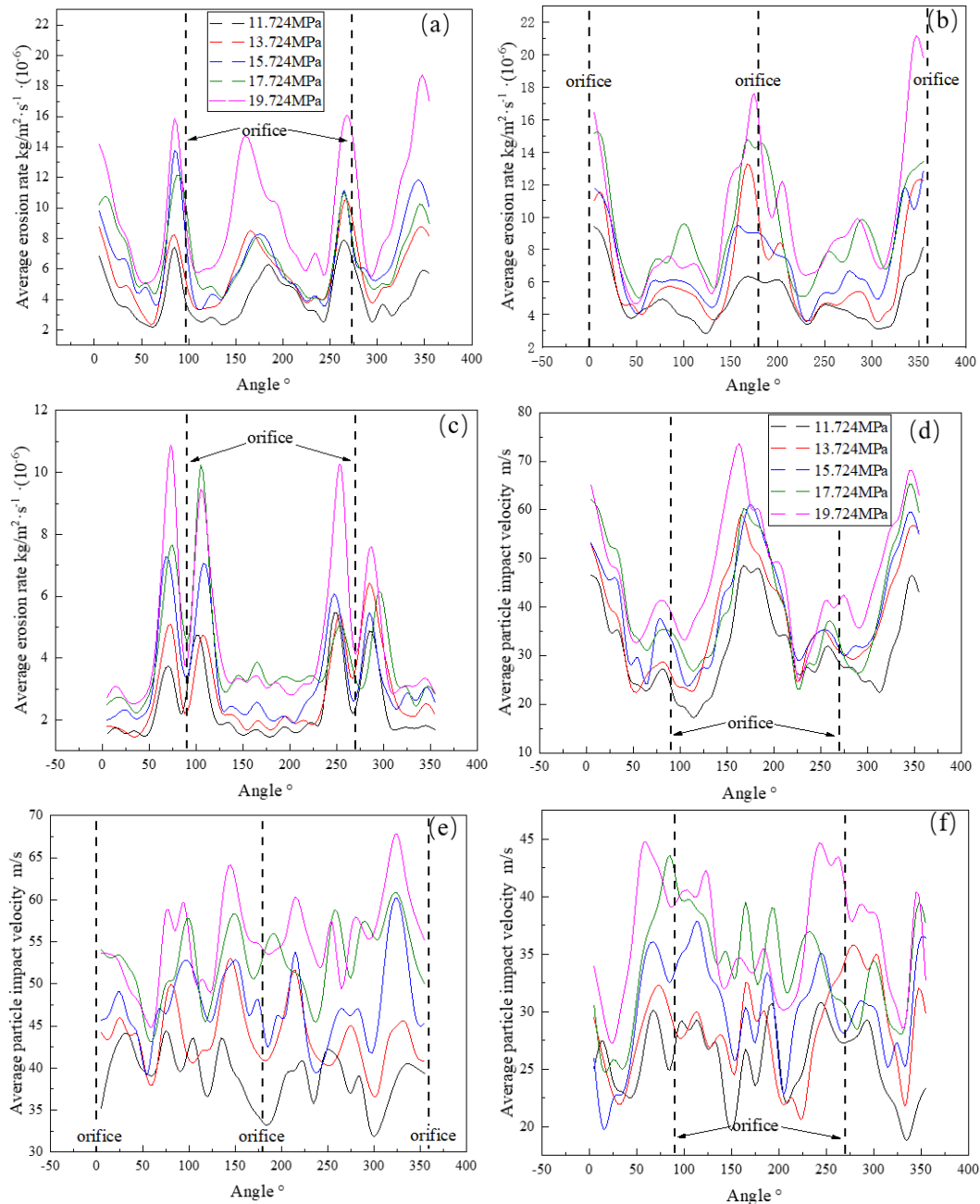


Fig. 15. Comparison of erosion profiles and particle impact velocities of cylinders with varying differences in pressure.

For bevels 2 and 3, when the sizes of the opening were 80%–35%, the area of high erosion was concentrated at the bottom and the range of erosion expanded in the longitudinal direction. Particles started to decelerate, and did not have a sufficiently high velocity to reach the top of the face of the bevel because of collisions, rebounding, and the decay in kinetic energy caused by turbulence in the AFC. Moreover, the difference in velocity between phases decreased compared with that of bevel 1, resulting a lower impact velocity of the particles as shown in Fig. 14 (c). The particle impact velocity at the top of bevel was higher, and was contrary to the erosion distribution there. Figure 14(b) shows that the mass concentration of the particles was consistent with

that of erosion, which means that the mass of the impacting particles was the dominant factor influencing erosion.

3.2 Pressure difference

In this section, we study the influence of varying differences in pressure between the front and back of the valve on the characteristics of erosion of the valve at a fixed size of the opening of 50%. The differences in pressure were 11.724 MPa, 13.724 MPa, 15.724 MPa, 17.724 MPa, and 19.724 MPa.

3.2.1 Annular flow channel

Figures 15 (a)–(f) show the erosion morphology of

the cylinder under annular flow and varying differences in pressure between the front and back of the valve. Figure 15(a) shows that five points at which severe erosion occurred were obtained under the five magnitudes of differences in pressure. This is because the greater difference in pressure contributed to the velocity of particle impingement and reduce the thickness of the protective fluid film, which caused more significant erosion even at a point of high mass concentration deviating by 90° from the exit of the throttling channel. Figures 15(b) and (c) show that with the increase in the difference in pressure, erosion gradually deepened. The difference in the rates of erosion between various values of differences in pressure is higher in Fig. 15 (c). This can be attributed to greater pressure and the dissipation of kinetic energy after the two throttling processes, because of which erosion was concentrated at the exit of the throttling section.

Figures 15(a)–(c) show that erosion became more concentrated along the direction of flow, and the number of points at which significant erosion occurred decreased from five to two after the first throttling channel. In Section 3.1.1, we reported a higher turbulence intensity in the annular flow channel and a cavity in the throttling section (O2 and O3), which led to more particles undergoing random motion and a deceleration in their impact velocity. Figures 15(d)–(f) shows the curves of distribution of

the particle impact velocity. For cylinders 2 and 3, they had no clear pattern, and the magnitude of velocity of particles in cylinder 2 was lower than that of cylinder 1.

3.2.2 Throttling flow channel

Figure 16 shows the erosion distribution along the direction of flow at the flat and the bevel. With the increase in the difference in pressure, the zone of severe erosion in bevels 1–3 (Figs. 16(a)–(b)) gradually became concentrated at the bottom and its maximum value gradually increased. When the difference in pressure was less than or equal to 15.724 MPa, the rates of erosion were close to one another, especially at 13.724 MPa and 15.724 MPa. When the difference in pressure was greater than 15.724 MPa, the amplitude of erosion increased prominently and the change in it was more rapid along the direction of flow. This was due to an increase in the difference in pressure when passing through the throttling section. As the velocity of fluid increased, the Stokes number did as well, and the effect of the drag force on the particles decreased. This caused the particles to tend to gather and strike the wall directly, thus producing a more concentrated erosion on the bevel. When the difference in pressure was smaller, the flow velocity of the continuous phase was lower, which means that the Stokes number was small and particles tended to disperse with the fluid, resulting in extensive wear.

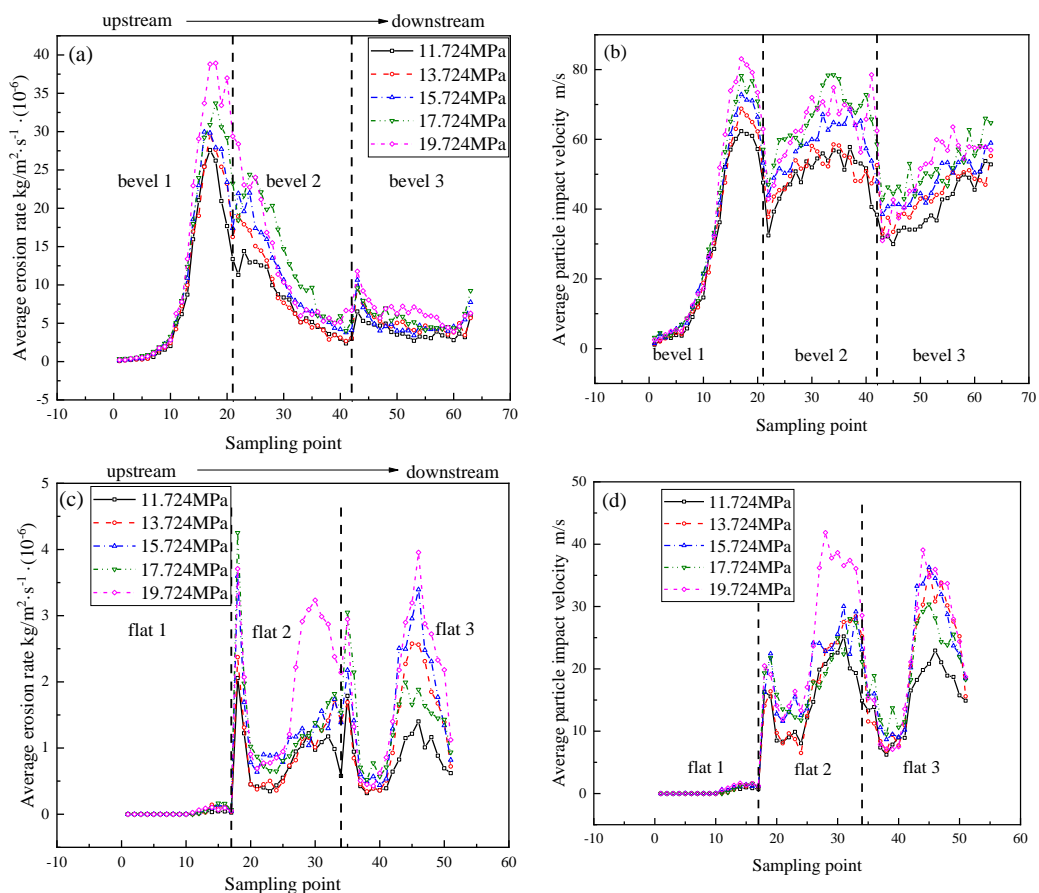


Fig. 16. Distributions of erosion and particle impact velocity with varying differences in pressure.

It is clear from Figs. 16(c) and (d) that when the difference in pressure was lower than 19.724 MPa, the increases in the rate of erosion and particle impact velocity of the flat were not in direct proportion to it, and were even lower than those at 11.724 MPa and 13.724 MPa. In addition, the difference in the rates of erosion among the four conditions was small for flat 2, except at 19.724 MPa. Figure 16(d) shows that particles hitting the top of the flat had a higher impact velocity than those striking the bottom because the fluid carrying particles hitting the top accelerated when flowing through the corner at the end of the annular flow channels.

4. CONCLUSIONS

In this paper, the authors used the CFD-DEM to simulate the characteristics of erosion of a multistage pressure relief string-regulating valve by considering the influence of the size of its opening and differences in pressure on the erosion distribution. The conclusions are as follows:

1. In case of openings of different sizes, the effects of throttling and depressurizing of the BO and OO were different. The locations of the throttling and depressurizing points gradually changed from the OO to the BO with the increase in the size of the opening. A large amount of mechanical energy of the fluid dissipated in the three throttling channels with a stair and slope-type structure, which contributed to the high turbulence intensity. The annular flow channel (AFC), and the cavity between the BO and OO provided space for the formation of a zone of high turbulence intensity and a buffer zone.

2. For openings of 80% and 20%, the area of flow of the orifices of the OO and BO decreased, resulting in more concentrated erosion. With a reduction in the size of the opening, the areas where a large amount of erosion had occurred decreased in the flat. The particles eroded the entire surface in the region with a large velocity gradient on the face of the bevel owing to different flow patterns. With the development of a high turbulence intensity, the particles lost some of their kinetic energy and erosion became more concentrated at several fixed points downstream.

3. With an increase in the differences in pressure, the depth of erosion significantly increased in each part of the valve. The velocity of flow was higher, and caused some particles to break away from the fluid. This led to the aggregation of particles and more concentrated erosion. A large difference in pressure enhanced the instability of the particle distribution, causing random particle collisions and an increase in the range of erosion, especially on the faces of the flat and the cylinder.

The proposed multistage depressurization string structure can disperse erosion in all parts of the throttle element, and does not cause excessive local wear. Moreover, the multistage pressure-relief structure can ensure the stability of depressurization and a higher accuracy of flow regulation. However,

while it reduces erosion, this causes more serious erosion in the first throttling section than the other sections. Future research should thus seek ways to increase its wear-resistance. Moreover, because the WC-Co material eroded severely when the angle of incidence of the particles was larger than 75°, research should also focus on reducing the impact angle of the high-speed fluid or particles by as much as possible. The buffer zone in the throttling channels can provide a high turbulence intensity, which should be used for more efficient energy dissipation. However, excessive turbulence can cause low local pressures and an increase in the threshold pressure for phase change, which may result in severe cavitation.

ACKNOWLEDGMENT

This work was supported by the National Key R&D Program of China (2018YFB2004002).

REFERENCE

- Akhshik, S., M. Behzad and M. Rajabi (2016). CFD-DEM simulation of the hole cleaning process in a deviated well drilling: The effects of particle shape. *Particuology* 25(02), 72-82.
- Akhshik, S. and M. Rajabi (2021). Simulation of proppant transport at intersection of hydraulic fracture and natural fracture of wellbores using CFD-DEM. *Particuology* 63, 112-124.
- Bernt, O. J. and O. S. Bengt (1972). Determination of young's modulus and poisson's ratio for WC-Co alloys by the finite element method. *Materials Science and Engineering* 9, 217-222.
- Cao, L., S. Liu, P. Hu and H. Si (2020). The influence of governing valve opening on the erosion characteristics of solid particle in steam turbine. *Engineering Failure Analysis* 118, No.104929.
- Charles, A. L., K. Chelvakumar, C. E. Brennen and A. J. Acosta (1981). Synfuel systems. a review of letdown devices and other multiphase flow problems. *california institute of technology*.
- Chen, J., Y. Wang, X. Li, R. He and Y. Chen (2015). Erosion prediction of liquid-particle two-phase flow in pipeline elbows via CFD-DEM coupling method. *Powder Technology* 275, 182-187.
- Chen, X. Z. and J. W. Wang (2014). A comparison of two-fluid model, dense discrete particle model and CFD-DEM method for modeling impinging gas-solid flows. *Powder Technology* 254, 94-102.
- Chu, Y., Z. Yuan and W. Chang (2020). Research on the Dynamic Erosion Wear Characteristics of a Nozzle Flapper Pressure Servo Valve Used in Aircraft Brake System. *Mathematical Problems in Engineering*.
- Darihaki, F., E. Hajidavalloo, A. Ghasemzadeh and G. A. Safian (2017). Erosion prediction for

- slurry flow in choke geometry. *Wear* 372-373, 42-53.
- Du, H., Q. B. Wu, H. Chen and L. Wang (2014). The Design and Analysis of Novel High-Flow Filling Valve based on Multi-Stage Hydraulic Resistance and Compound Flow Channels. *International Journal of Control & Automation* 7(9), 433-450.
- Jin, H., Z. Zheng, G. Ou, L. Zhang, J. Rao, G. Shu and C. Wang (2015). Failure analysis of a high-pressure differential regulating valve in coal liquefaction. *Engineering Failure Analysis* 55, 15-130.
- Johnson, K. L. (1985). *Contact Mechanics*. Cambridge University Press, Cambridge, England.
- Krishnan, R. P. (1984). Assessment of slurry pressure letdown valve and slurry block valve technology for direct coal liquefaction demonstration and pioneer commercial plants.
- Landau, L. D. and E. M. Lifshitz (1970). *Theory of Elasticity*. Pergamon Press, New York.
- Lin, Z., X. Sun, T. Yu, Y. Zhang, Y. L. Li and Z. Zhu (2020). Gas–solid two-phase flow and erosion calculation of gate valve based on the CFD-DEM model. *Powder Technology* 366, 395-407.
- Liu, B., J. Zhao and J. Qian (2017). Numerical analysis of cavitation erosion and particle erosion in butterfly valve. *Engineering Failure Analysis* 80, 312-324.
- Liu, J. G., G. S. Wang, T. H. Peng, and S. Q. Jiang (2019). Numerical Simulation of Solid Particle Erosion in Aluminum Alloy Spool Valve. *Mathematical Problems in Engineering* 2, 1-16.
- Liu, X. F., J. F. Zhou, S. Q. Gao, H. L. Zhao, Z. Y. Liao, H. Z. Jin and C. Wang (2022). Study on the Impact Wear Characteristics of Catalyst. *Journal of Applied Fluid Mechanics* 15(1), 221-230.
- Mansouri, A. (2016). *A Combined CFD-Experimental Method for Developing an EROSION Equation for both Gas-Sand and Liquid-Sand Flows*, PhD Dissertation, Department of Mechanical Engineering, The University of Tulsa.
- McLaury, B. S. (1996). *Predicting solid particle erosion resulting from turbulent fluctuations in oilfield geometries*, PhD Dissertation, Mechanical Engineering, University of Tulsa.
- Messa, G. V., G. Ferrarese and S. Malavasi (2015). A mixed Euler–Euler/Euler–Lagrange approach to erosion prediction. *Wear* 342-343, 138-153.
- Mindlin, R. D. (1949). Compliance of Elastic Bodies in Contact. *Journal of Applied Mechanics* 16, 259-268.
- Morsi, S. A. and A. J. Alexander, (1972). An investigation of particle trajectories in two-phase flow systems. *Journal of Fluid Mechanics* 55(2), 193-208.
- Paggiaro, R., J. D. Friedemann, E. Gharaibah and Y. Zhang (2013). Prediction of Sand Erosion in Choke Valves - CFD Model Development and Validation against Experiment. *offshore technology conference Brasil*.
- Qian, J. Y., M. Zhang, L. N. Lei, F. Q. Chen, L. L. Chen, L. Wei and Z.J. Jin (2016). Mach number analysis on multi-stage perforated plates in high pressure reducing valve. *Energy Conversion and Management* 119, 81-90.
- Varga, M., C. Goniva, K. Adam and E. Badisch (2013). Combined experimental and numerical approach for wear prediction in feed pipes. *Tribology International* 65(3), 200-206.
- Wang, C., A. Q. Duan and K. N. Bi (2021). Experiment on Erosion Wear Characteristic of NiWC35 Coating and Sintered WC under High-Speed Impacting of Solid Particle. *Journal of Applied Fluid Mechanics* 14(4), 1125-1136.
- Wang, G. R., F. Chu, S. Tao, L. Jiang and H. Zhu (2015). Optimization design for throttle valve of managed pressure drilling based on CFD erosion simulation and response surface methodology. *Wear* 338-339, 114-121.
- Wang, H. M., Y. Zhao, J. X. Wang, X.S. Kong, H. Liu, K.L. Li and X. F. Wang (2016). Numerical simulation of flow characteristics for a labyrinth passage in a pressure valve. *Journal of Hydrodynamics*, Ser. B, 28(4), 629-636.
- Yan, H., J. Li, C. Cai and Y. Ren (2020). Numerical Investigation of Erosion Wear in the Hydraulic Amplifier of the Deflector Jet Servo Valve. *Applied Sciences* 10(4), 1299.
- Zheng, S., M. Luo, K. Xu, X. Li and Z. Liu (2019). Case study: Erosion of an axial flow regulating valve in a solid-gas pipe flow. *Wear* 434-435, No.20952.
- Zheng, Z., G. Ou, Y. Yi, G. Shu and H. Ye (2016). A combined numerical-experiment investigation on the failure of a pressure relief valve in coal liquefaction. *Engineering Failure Analysis* 60, 326-340.
- Zhou, J. W., Y. Liu, S. Y. Liu, C. L. Du and J. P. Li (2017). Effects of particle shape and swirling intensity on elbow erosion in dilute-phase pneumatic conveying. *Wear* 380-381, 66-77.